Plasma Physics and Controlled Fusion

OPEN ACCESS

RECEIVED
31 December 2025

REVISED
31 March 2026

ACCEPTED FOR PUBLICATION
10 April 2026

PUBLISHED
29 April 2026

PAPER

Enabling energy-doubling at CLARA FEBE: high-quality beam generation in plasma wakefield acceleration

Jiaqi Zhang[1,2], **Deepa Angal-Kalinin**[3,2], **Oznur Apsimon**[1,2], **Stewart Boogert**[1,2], **Richard D'Arcy**[4], **James Jones**[3,2], **Toby Overton**[3,2], **Thomas Pacey**[3,2], **Hossein Saberi**[1,2] and **Guoxing Xia**[1,2,*]

[1] Department of Physics and Astronomy, University of Manchester, Manchester, United Kingdom
[2] Cockcroft Institute, Warrington, United Kingdom
[3] Accelerator Science and Technology Centre (ASTeC), STFC Daresbury Laboratory, Warrington, United Kingdom
[4] John Adams Institute, University of Oxford, Oxford, United Kingdom
[*] Author to whom any correspondence should be addressed.

E-mail: guoxing.xia@manchester.ac.uk and jiaqi.zhang@manchester.ac.uk

Keywords: plasma wakefield acceleration, CLARA FEBE, particle-in-cell, plasma density ramp, beam loading

Abstract

Plasma-wakefield acceleration (PWFA) has attracted great attention due to its high accelerating gradients, which will drastically reduce the price, footprint, and carbon load of accelerators to be used for medical applications, free electron lasers (FELs), and future high-energy physics experiments. The compact linear accelerator for research and applications (CLARA) at the Daresbury Laboratory is a state-of-the-art electron accelerator for a future FEL test facility, capable of producing 250MeV electron bunches. Recently, a new beamline attached to CLARA, the so-called full energy beam exploitation (FEBE) facility, has been commissioned to provide ultra-short and low-emittance electron bunches. Here, we use the Fourier–Bessel particle-in-cell code to investigate PWFA with a two-bunch configuration at FEBE, aiming to double the energy of the witness bunch while preserving its incoming beam quality. Simulation results indicate that the driver's trailing portion is tightly focused by the transverse wakefield, leading to a surging beam density and a transition from the linear to the non-linear regime. An appropriate flattened wakefield due to beam loading is achieved assisted with the tailoring of the plasma density. Moreover, the impact of ramping plasma density on beam quality is also discussed.

1. Introduction

Plasma-based acceleration, first proposed in a seminal paper in 1979 by Tajima and Dawson [1], has emerged as a promising solution to the limitations of conventional radio-frequency (RF) based accelerators, including their large scale, high cost, and significant carbon footprint. Plasma wakefield acceleration (PWFA) provides a more compact alternative, offering accelerating gradients that are 1–3 orders of magnitude higher than conventional RF-based accelerators [2]. In addition, PWFA benefits from longer dephasing lengths [3] and drive-to-witness energy-transfer efficiency [4], all of which have attracted considerable attention from the accelerator community in recent decades [2].

The first proof-of-principle PWFA experiment was conducted at Argonne national laboratory, demonstrating an accelerating gradient of 1.6 MeV m^{-1} [5]. In 2007, researchers at the Stanford Linear Accelerator Center (SLAC) injected a single 42 GeV electron bunch into a plasma and achieved energy doubling of the rear part of electrons with an 85-cm-long plasma column produced in a heat-pipe oven [6], corresponding to an accelerating gradient of approximately 52 GeV m^{-1}. The driver-witness configuration was subsequently introduced [7], employing two-bunch generation methods such as notch/-jaw collimators (FACET, SLAC) [8] and wedge/block collimators (FLASHForward, DESY) [9]. Since then, research efforts have increasingly focused on achieving high beam quality [10] and high energy-transfer efficiency [11] to meet the demanding requirements of high-energy physics experiments [12], free-electron lasers (FELs) [13], and beam radiation therapy [14].

Energy doubling experiments have primarily focused on maximising the accelerating gradient, which is constrained by the plasma wave-breaking limit, also referred to as the cold non-relativistic wave-breaking field in the linear regime [15], expressed as $E_{\max}\ [\mathrm{V\,m^{-1}}] = m_e\ \mathrm{c}\ \omega_p/e \approx 96\ n_0^{1/2}\ [\mathrm{cm^{-3}}]$, where m_e, c, ω_p, e, and n_0 represent the electron mass, speed of light in vacuum, plasma frequency, electron charge, and initial plasma density, respectively. In particular, under the strong focusing condition, where $k_p\sigma_z = \sqrt{2}$ and $k_p\sigma_r \ll 1$, the accelerating gradient can be predicted as a driver-dependent function in the linear regime [16]:

$$E_{\max,\mathrm{lin}}\left[\mathrm{MV\ m^{-1}}\right] \approx 240\left(\frac{N_b}{4\times10^{10}}\right)\left(\frac{600}{\sigma_z[\mu\mathrm{m}]}\right)^2, \tag{1}$$

where k_p is the plasma wavenumber, N_b is the number of electrons in the drive bunch, σ_z is the (root-mean-square) rms bunch length and σ_r is the rms bunch radius. Therefore, the parameters of the driver can significantly determine the acceleration performance. On the other hand, beam quality, typically characterised by the charge loss during acceleration, energy spread, emittance, peak current, and other related factors [13], is often compromised when optimising the acceleration gradient. For example, employing a low plasma density helps achieve a more uniform wakefield along the propagation direction and can reduce the energy spread to an acceptable level. However, according to the wave-breaking limit, the resulting acceleration gradient tends to be modest. Therefore, identifying an appropriate strategy that simultaneously achieves a high acceleration gradient and beam quality preservation, is of great importance for advancing the practical applications of PWFA.

In recent studies, a down-ramp plasma density profile has been introduced in LWFA to attract more self-injection electrons, since the phase velocity of the plasma bubble is reduced, as theoretically demonstrated in [17]. For proton-driven PWFA, an up-ramp plasma profile has been shown to stabilise the wakefield [18]. For PWFA, the plasma density transition, has also been widely employed to tailor the transverse focusing forces during beam propagation, which has been shown to help preserve the beam emittance through mechanisms such as space-charge–assisted damping [19], plasma–beam mismatch [20], hose instability [21], and chromatic phase spread [22]. As well as emittance reduction, the periodic plasma density transition can be used to preserve the energy spread in the linear regime [23]. In this paper, we investigate how plasma density ramps within the acceleration stage influence the preservation of multiple beam-quality metrics, with the aim to achieve high-quality energy-doubled electron beam for future applications.

The compact linear accelerator for research and applications (CLARA) at the Daresbury Laboratory [24] is a state-of-the-art electron accelerator designed as a future testbed for FELs. It is capable of producing 250-MeV electron bunches. Recently, a new beamline attached to CLARA, the full energy beam exploitation (FEBE) facility, has been successfully commissioned to deliver ultra-short and low-emittance electron bunches for users. In this paper, we perform simulation studies of PWFA for energy doubling at CLARA FEBE. Through the use of coupled up-ramp and down-ramp plasma profiles, particle-in-cell (PIC) simulations indicate that the energy of the witness beam can be doubled within a 20-cm-long plasma cell, while the beam quality remains nearly preserved.

This paper is organised as follows. Section 2 provides an overview of the CLARA facility and its beam specifications. Section 3 introduces the PIC simulation framework and the parametric settings. Section 4 demonstrates the transition to the non-linear regime and the beam loading effect, and discusses the influence of the plasma density ramps on beam quality. Finally, key findings are summarised in section 5.

2. CLARA FEBE beam for PWFA

2.1. Layout for PWFA

The schematic layout of the PWFA experiment is shown in figure 1. The beamline can be divided into three sections: two-bunch generation and shaping, experimental hutch, and diagnostics. Two-bunch generation is carried out in the beam-shaping section using a mask that is inserted at the midpoint of a magnetic chicane, where it scatters electrons to create a spatial separation between the bunches. Subsequently, the driver and witness beams propagate through the experimental region, where the plasma is generated by the capillary discharge. To produce the ramping plasma profile, two discharge cathode plates connected to a pump can be installed at both ends of the plasma capillary. Finally, the downstream section hosts a variety of beam diagnostics and beam dump facilities for beam quality measurement and energy dissipation.

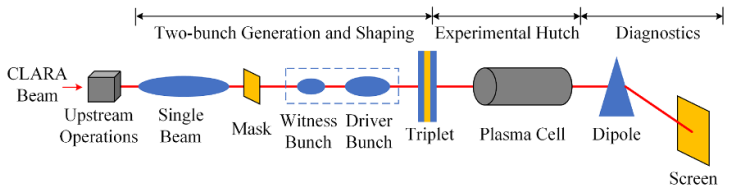

Figure 1. Schematic layout for PWFA with FEBE beamline.

2.2. FEBE beam specifications

The specifications of the CLARA beam were reported in [24]. An electron beam with an energy of up to 250 MeV can be generated from upstream CLARA operations. Two main beam modes are available, i.e. the high-charge (250 pC) and low-charge (5 pC) modes. FEBE offers flexibility with the available bunch charge from 5 to 250 pC. Note that the low-charge mode is preferred for generating shorter bunches, due to weaker space-charge effects at a low energy (below 35 MeV at the CLARA front end) and fewer limitations in beam compression (coherent synchrotron radiation effect). The beam compression monitor is expected to measure the minimum rms bunch lengths of < 50 fs for a 100 pC bunch. For the transverse size, the nominal commissioning beam for the high-charge mode is 100 μm and will be further reduced to 50 μm through machine development in support of novel acceleration research and development (R&D). In addition, a typical high-charge electron beam is expected to have an energy spread of roughly 1% and a normalised emittance of 5 mm mrad.

3. Simulation model and parameters

3.1. Numerical setup

the Fourier–Bessel PIC (FBPIC) code [25] is employed to solve cylindrical problems. FBPIC is a quasi-three-dimensional code that solves the Maxwell's equations, where the azimuthal mode m ($m = 0$, 1, 2, …) can be specified to represent the electromagnetic field distribution. For instance, $m = 0$ corresponds to an axisymmetric field that are independent of the azimuthal angle θ in cylindrical coordinates. The $m = 1$ mode represents the fields that vary proportionally to $\cos\theta$ and $\sin\theta$, which is the case for a linearly polarised laser pulse in laser wakefield acceleration simulations. High-order modes ($m > 1$) of represent the fields that vary proportionally to $\cos(m\theta)$ and $\sin(m\theta)$, which can be used to model further departures from the cylindrical symmetry. The background ions are assumed to be immobile during the simulation. The key strength of FBPIC lies in its coupling of the cylindrical coordinate system with spectral PIC algorithms, which can efficiently handle computationally intensive problems and minimise spurious numerical dispersion [25–27].

Table 1 summarises the main numerical parameters used in the FBPIC simulations. The simulations are performed in a moving window of 150 μm in both the longitudinal and transverse directions, initialised with 500 $\times$ 200 grid cells in (z, r). This corresponds to fixed spatial resolutions of $\Delta z = 0.30$ μm and $\Delta r = 0.75$ μm, i.e. $\Delta z = (0.009 - 0.012) \times k_{\mathrm{p}}^{-1}$ and $\Delta r = (0.024 - 0.029) \times k_{\mathrm{p}}^{-1}$, where the range reflects the variation of k_{p} associated with the plasma-density ramp rather than a change in the grid itself. The grid spacing resolves the plasma skin depth k_{p}^{-1} with multiple cells, ensuring accurate representation of the wakefield structure and beam–plasma interaction. The time step is chosen as $\Delta t = \Delta z/c = 1.0$ fs, consistent with the pseudo-spectral analytical time-domain scheme employed by FBPIC and free of a Courant stability limit. Each cell contains $n_r \times n_z \times n_\theta = 4 \times 4 \times 4$ macroparticles to maintain computational efficiency. The boundaries of the simulation window are reflective in the radial (r) direction and open in the longitudinal (z) direction.

Note that the physical scenario is modelled using a purely cylindrical azimuthal mode $m = 0$. The drive and witness beams are initialised without transverse offset, with identical transverse size ($\sigma_x = \sigma_y$) and normalised emittance ($\epsilon_{N,x} = \epsilon_{N,y}$). We performed simulations including higher-order azimuthal modes and evaluated the weighted, slice-averaged fields experienced by both the drive and witness beams. The results show that the ratios of higher-order modes to the $m = 0$ mode are nearly zero, indicating that the contribution of higher-order azimuthal modes to the wakefields is negligible. Therefore, the axisymmetric configuration adopted here is sufficient to capture the physical scenario.

Table 1. Numerical parameters used in the FBPIC simulations.

Parameters	Values
Longitudinal window size	$150\,\mu$m
Transverse window size	$150\,\mu$m
Number of grid cells ($N_z \times N_r$)	500×200
Longitudinal cell size (Δz)	$0.30\,\mu\text{m}\ (0.009 - 0.012) \times k_\text{p}^{-1}$
Radial cell size (Δr)	$0.75\,\mu\text{m}\ (0.024 - 0.029) \times k_\text{p}^{-1}$
Azimuthal mode (m)	0
Time step (Δt)	1.0 fs
Macroparticles per cell	$4 \times 4 \times 4$
Boundary conditions	Radial: reflective. Longitudinal: open

Table 2. Employed beam and plasma parameters for the PWFA study.

Parameters	Driver	Longer witness	Shorter witness
Plasma density (cm^{-3})	N/A	$2.8\text{–}4.2 \times 10^{16}$	$1.9\text{–}4.2 \times 10^{16}$
Beam density (cm^{-3})	1.19×10^{15}	1.98×10^{15}	1.98×10^{16}
Driver-witness separation (μm)	N/A	90	90
Charge (pC)	150	10	5
Energy (MeV)	250	250	250
Bunch length (μm)	10	10	2
Transverse size (μm)	70	14	7
Energy spread (%)	1	1	1
Emittance (mm mrad)	5	5	2

3.2. Beam and plasma parameters

Table 2 lists the beam and plasma parameters employed in this work. The single beam from the FEBE carries a charge of 250 pC. When the beam propagates through the tungsten mask, the central electrons are scattered, thereby generating a drive-witness bunch pair with variable delay. Here, we refer to the SLAC notch collimator, where approximately 60% of the electrons remain after the collimation [4]. Therefore, we set 150 pC to the driver, 10 pC (64% remaining) to the longer witness beam, and 5 pC (62% remaining) to the shorter witness beam.

The bi-Gaussian beam density distribution for the two-bunch configuration is traditionally assumed, given by

$$n_{\boldsymbol{b}}(r,\xi) = \frac{Q/e}{(2\pi)^{3/2}\sigma_z\sigma_r^2}\exp\left(-\frac{r^2}{2\sigma_r^2}\right)\exp\left(-\frac{\xi^2}{2\sigma_z^2}\right), \tag{2}$$

where Q, σ_z, σ_r, $\xi = z—ct$ represent the bunch charge, bunch length, bunch radius, and the co-moving longitudinal coordinate, respectively. We initialise the bunch lengths $\sigma_{z,\text{dri}} = 10\,\mu$m and $\sigma_{z,\text{wit}} = 10\,\mu$m, and the transverse sizes as $\sigma_{x,\text{dri}} = 70\,\mu$m and $\sigma_{x,\text{wit}} = 14\,\mu$m. The energy spread for all beams is set to 1%. A shorter witness beam ($\sigma_{z,\text{wit}} = 2\,\mu$m, $\sigma_{x,\text{wit}} = 7\,\mu$m, normalised projected rms emittance $\epsilon_\text{N} = 2$ mm mrad) is set by reducing the charge, while remaining within the operational range of the low-charge mode of the FEBE. The driver density of $n_\text{b} = 1.19 \times 10^{15}\,\text{cm}^{-3} \ll n_0$ ($2.8 \times 10^{16}\,\text{cm}^{-3}$ for the longer witness bunch and $1.9 \times 10^{16}\,\text{cm}^{-3}$ for the shorter witness bunch) indicates an over-dense plasma environment. In addition, the initial driver–witness separation is defined as the longitudinal distance between the centroids of the drive and witness beams and is optimised through parameter scans by evaluating the resulting beam quality. Previous studies typically adopted a separation in the range of 0.5–1.0 λ_p [28–30]. Through optimisation within this range, the separation in this work is determined to be 90 μm, corresponding to 55% of the plasma wavelength behind the driver at the maximum plasma density $4.2 \times 10^{16}\,\text{cm}^{-3}$. This optimal result is consistent with the condition that the witness beam simultaneously remains in the accelerating and focusing plasma phases.

Figure 2 shows the ramping helium plasma density profile used in this work, divided into five stages: an initial stage, an up-ramp, a high-density plateau, a down-ramp, and a final low-density stage. Each stage of the profile is designed with consideration of both theoretical principles and practical limits. Before the plasma enters the up-ramp stage, the witness beam is focused by the transverse wakefield, as will be discussed in section 4.1. The focusing effect brings the witness beam closer to satisfying the

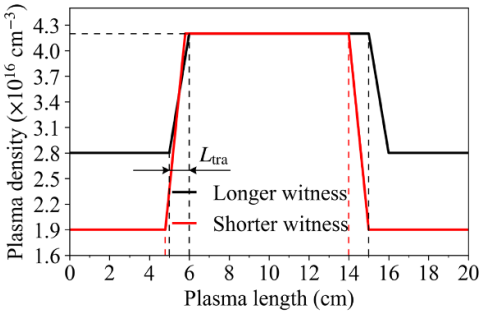

Figure 2. Ramping plasma density profiles for two witness beam parameter sets.

emittance preservation condition [31, 32]:

$$\sigma_{x,y,\boldsymbol{mat}} = \left(\frac{2c^2\varepsilon_N^2 m_e \varepsilon_0}{n_0 e^2 \gamma}\right)^{1/4}, \tag{3}$$

where ϵ_N, ϵ_0, n_0, and γ represent the initial normalised emittance, vacuum permittivity, plasma density, and initial Lorentz factor of the witness beam, respectively.

The plasma density ramp is assumed to be linear [30, 33], with its mathematical expression defined as follows:

$$n_p(z) = \begin{cases} n_0 & \text{for} \quad 0 \leqslant z < z_{up}, \\ n_0 + (n_{max} - n_0)\dfrac{z - z_{up}}{L_{up}} & \text{for} \quad z_{up} \leqslant z < z_{up} + L_{up}, \\ n_{max} & \text{for} \quad z_{up} + L_{up} \leqslant z < z_{down}, \\ n_{max} + (n_0 - n_{max})\dfrac{z - z_{down}}{L_{down}} & \text{for} \quad z_{down} \leqslant z < z_{down} + L_{down}, \\ n_0 & \text{for} \quad z \geqslant z_{down} + L_{down}. \end{cases} \tag{4}$$

where n_0 denotes the initial plasma density, which is $2.8 \times 10^{16}\,\mathrm{cm}^{-3}$ and $1.9 \times 10^{16}\,\mathrm{cm}^{-3}$ for the longer and shorter witness bunches, respectively. $n_{max} = 4.2 \times 10^{16}\,\mathrm{cm}^{-3}$ denotes the plasma density in the plateau stage. The positions z_{up} and z_{down} denote the starting locations of the up-ramp and down-ramp, respectively, while L_{up} and L_{down} denote the corresponding ramping lengths.

Regarding the density transition length, previous studies have demonstrated that a quasi-monoenergetic beam can be produced when the transition is sufficiently sharp, i.e. when $L_{tra} < \lambda_p$ [17], where L_{tra} denotes the ramp length and λ_p denotes the plasma wavelength. However, theoretical investigations of sharp transitions for externally injected beams have not been well documented. Therefore, this work focuses mainly on practical considerations. A discharge capillary technique has been demonstrated over a few centimetres at SPARC_LAB [34–36], DESY [37], and BELLA [38]. According to these results, the typical ramping length for capillary-based plasma sources is on the order of ∼1 cm, providing a valuable reference for the design of the plasma cell in PWFA experiments at FEBE. Therefore, we initialise a 1-cm-long plasma density ramps in the simulations, i.e. $L_{up} = L_{down} = 1\,\mathrm{cm}$.

The peak density and the final-stage density are determined through parameter scans. A lower peak density requires a longer plasma cell for energy doubling, which results in longer length for beam quality recovery (see section 4.3.4) during the final low-density plasma stage. Therefore, we selected the up-ramp point $z_{up} = 5\,\mathrm{cm}$ and down-ramp point $z_{down} = 15\,\mathrm{cm}$ for the longer witness beam. The corresponding positions for the shorter witness beam are $z_{up} = 4.8\,\mathrm{cm}$ and $z_{down} = 14\,\mathrm{cm}$.

It is important to select an appropriate plasma density range, where the witness beam can be accelerated and focused. The plasma density range is determined by the variation in plasma wavelength, expressed as $\Delta\lambda_p = \lambda_p(1 - (n_{01}/n_{02})^{0.5})$ [17], where n_{01} and n_{02} denote the lower and upper bounds of the plasma density, respectively. $\lambda_p = 2\pi c/\omega_p$ denotes plasma wavelength, where $\omega_p = (n_0 e^2/m_e\epsilon_0)^{1/2}$ represents the plasma frequency. For shorter wavelengths, the rear part of witness electrons may enter the defocusing phase of the dephasing regime, leading to a significant charge loss. While for longer wavelengths, the front part of witness electrons may experience the decelerating phase of the dephasing regime. As a result, the energy spread inevitably grows significantly. Parameter scan results indicate that the optimal plasma density lies within $2.8\text{–}4.2 \times 10^{16}\,\mathrm{cm}^{-3}$ for the longer witness bunch and $1.9\text{–}4.2 \times 10^{16}\,\mathrm{cm}^{-3}$ for the shorter witness bunch.

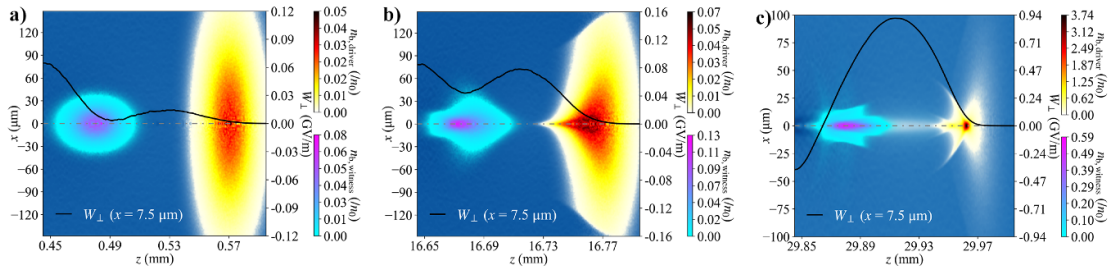

Figure 3. The driver is focused by the transverse wakefield inside the uniform plasma density 4.2×10^{16} cm^{-3} at (a) $z = 0.57$ mm, (b) $z = 16.77$ mm, and (c) $z = 29.97$ mm. Off-axis transverse wakefield was visualised because electrons in outer transverse regions experience nonlinear transverse forces and are more likely to enter the defocusing regime.

4. Simulation results

4.1. Non-linear regime transition

The density of the driver employed in this study is on the order of 10^{15} cm^{-3}. To achieve the maximum wakefield, the beam-plasma interaction must occur in the non-linear regime, which requires the plasma density to be comparable to or lower than 10^{15} cm^{-3}, according to the condition $n_b > n_0$. However, at this density scale, an accelerating field of several hundred MV m^{-1} can be obtained [39], corresponding to a plasma-cell length of 0.5–1.0 m for energy doubling, which is longer than what we originally expected in our research objectives.

Even for an initially low-density driver at the entrance to the plasma, PWFA can still evolve from the linear regime into the non-linear regime [40]. As the driver is focused by the transverse wakefield, a process commonly referred to as self-focusing effect, its density can increase by approximately one order of magnitude (to the 10^{16} cm^{-3} scale), as shown in figure 3. The front portion of the driver expels plasma electrons radially outward, forming a strong focusing transverse wakefield in its rear region. The front section, however, does not experience the focusing force immediately because the plasma requires a finite response time. The driver reaches a peak density of $3.74n_0$ at its centre, forming a long and narrow ion cavity in the plasma along the propagation direction. Note that the bubble regime (a strongly non-linear regime) requires $n_b \gg n_0$, the current acceleration mode corresponds to the quasi-nonlinear regime [41].

The transition to the nonlinear regime significantly increases the maximum transverse wakefield from ∼0.06 GV m^{-1} to ∼0.90 GV m^{-1} at the edge of the witness bunch and from ∼0.01 GV m^{-1} to ∼0.44 GV m^{-1} in the bunch centre, which instantly focuses the witness beam. The beam density rises by one order of magnitude, reaching $0.59n_0$ compared with the initial density of $0.08n_0$. On the other hand, with the increase of the plasma density, the boundary electrons in the rear section of the witness beam are defocused by the transverse wakefield of ∼0.19 GV m^{-1}, as shown in figure 3(c).

Note that, in principle, Gaussian profiles extend to infinity. Therefore, a truncation is applied to the beams, as shown in figure 3(a). However, the tails of the Gaussian distribution decay rapidly and can thus be considered negligible. Within our simulation window, the drive beam contains 98.3% of the total charge. With further extension of simulation window, the computational cost increases rapidly with the number of grid points along the radial direction due to the complexity of the Hankel transform algorithm.

4.2. Beam loading effect

When the driver expels plasma electrons away from the propagation axis, these electrons experience strong electrostatic forces induced by the ion cavity. The witness beam can also excite its own wakefield, which delays the return of background electrons towards the axis. Since the structure of the long, narrow ion cavity in the quasi-nonlinear regime, or the bubble cavity in the blowout regime, is elongated, the sinusoid-like wakefield distribution tends to be superposed. However, the beam loading effect does not consistently flatten the wakefield to reduce the energy spread unless the proper matching condition between the plasma density and the charge profile of the witness beam is satisfied. Specifically, the trapezoidal charge profile has been verified both theoretically and numerically as one of the optimal configurations for flattening the wakefield [42].

Figure 4 illustrates the beam loading effect with the plasma density ramp for the longer-witness simulation group. It is found that beam loading acts as a positive-slope effect when the plasma density ranges $2.8–3.6\times10^{16}$ cm^{-3}, during which the tail portion of the witness beam gains more energy than

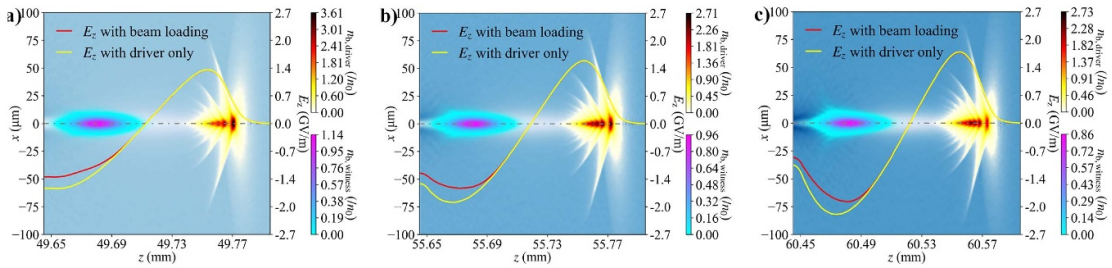

Figure 4. Beam density and on-axis ($x = 0$) wakefield using the plasma density ramp for the longer witness beam. The colour bar represents the ratio of beam density to the plasma density at the current simulation step, where (a) $n_0 = 2.8 \times 10^{16}$ cm^{-3}, (b) $n_0 = 3.6 \times 10^{16}$ cm^{-3}, and (c) $n_0 = 4.2 \times 10^{16}$ cm^{-3}.

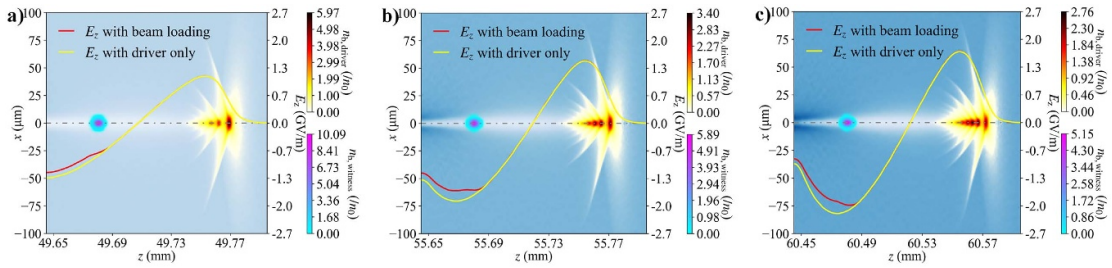

Figure 5. Beam density and on-axis ($x = 0$) wakefield using the plasma density ramp for the shorter witness beam. Current plasma density is (a) $n_0 = 1.9 \times 10^{16}$ cm^{-3}, (b) $n_0 = 3.2 \times 10^{16}$ cm^{-3}, and (c) $n_0 = 4.2 \times 10^{16}$ cm^{-3}, respectively.

the front portion. In contrast, an negative-slope effect occurs when the plasma density increases to $>$ 3.6×10^{16} cm^{-3}, where the tail portion of the witness beam experiences a lower acceleration gradient than the front portion.

Figure 5 shows a similar trend, with the transition from a positive-slope to a negative-slope effect occurring at approximately 3.2×10^{16} cm^{-3} for the shorter witness beam. In addition, the beam loading effect induced by the shorter witness beam is more uniform than that of the longer one. Therefore, the shorter beam demonstrates a more favourable charge distribution, benefiting from the beam loading effect in preserving the energy spread.

Note that the drive beam density ratio n_b/n_0 indicated in figure 5 correspond to the varying baseline plasma density. The ratio decreases from 5.97 in figure 5(a) and 3.40 in figure 5(b) to 2.76 in figure 5(c), reflecting the increasing background plasma density used for normalisation during the up-ramp stage rather than a physical reduction of the drive-beam density. On the contrary, the density essentially remains within $n_b = 1.0$–1.15×10^{17} cm^{-3}. Meanwhile, the peak density of the witness beam exhibits a slight increase, ranging from 3.19 to 3.61×10^{16} cm^{-3} for the longer witness beam and from 1.92 to 2.16×10^{16} cm^{-3} for the shorter one.

Interestingly, since the compensation status can be regulated by adjusting the plasma density, allocating specific plasma cell lengths for the positive-slope and negative-slope regions to counteract each other is feasible, even though the wakefield is not consistently uniform throughout the entire energy-doubling process. In this case, the front portion of the witness beam gains more energy before the transition point in the up-ramp stage, whereas the tail portion gains more energy after the transition point, primarily during the high-density section. Subsequently, after the transition point in the down-ramp stage, the front portion gains more energy once again. This mechanism represents one of the purposes of adopting the down-ramp plasma configuration. The energy spread is thereby re-corrected, corresponding to the beam quality recovery mentioned in section 3.2.

4.3. Transverse size and beam quality

4.3.1. Matching conditions

Although increasing the plasma density to the 10^{16} cm^{-3} can enhance the accelerating field to several GV m^{-1}, several major challenges arise. The reduced bubble size of the ion cavity leads to a shorter plasma wavelength, given by $\Delta\lambda_p = \lambda_p(1 - (n_{01}/n_{02})^{0.5})$ [17]. As a result, a higher plasma density narrows the matching region where the entire witness beam can be simultaneously accelerated and focused, to $\sim$ (λ_p—$\Delta\lambda_p$)/4 in the longitudinal direction [40], thereby increasing the susceptibility of the beam

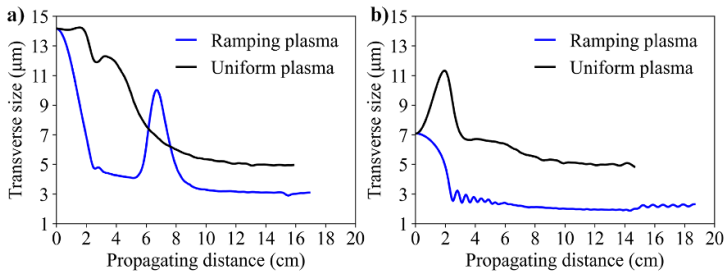

Figure 6. Bunch radius of (a) the longer witness bunch case and (b) the shorter witness bunch case. All data is collected within the 5σ range.

quality to degradation. Therefore, minimising the ratios σ_z/λ_p or σ_r/λ_p effectively increases the tolerance for matching acceleration conditions.

4.3.2. Transverse size and beam quality

Figure 6 shows the evolution of the transverse size for two witness bunch cases in uniform and ramping plasma, respectively. In the uniform plasma, the transverse size initially remains constant in the linear regime, then gradually shrinks and reaches an equilibrium state. In contrast, in the up-ramp plasma, the transverse size sharply shrinks at the beginning, triggers a single oscillation before settling to a smaller value than that in the uniform plasma.

Figure 6(b) further reveals that the transverse size in uniform plasma undergoes a single oscillation at the initial stage, whereas in the up-ramp plasma, it is sharply reduced and quickly stabilises, despite some small residual oscillations. As mentioned in section 3.2, parameter scan determined the up-ramp positions to be 5 cm and 4.8 cm for the longer and shorter witness bunch cases, respectively. The matched transverse sizes for 250 MeV electrons, calculated from equation (3) by substituting $n_0 = 2.8\times10^{16}$ cm^{-3} and $\epsilon_N = 5$ mm mrad for the longer witness bunch, as well as $n_0 = 1.9\times10^{16}$ cm^{-3} and $\epsilon_N = 2$ mm mrad for the shorter witness bunch, are 3.2 μm and 2.2 μm, corresponding to their individual up-ramp positions. Even when taking into account the energy gain of witness bunches (see figures 7(a) and 8(a)), e.g. $\gamma = 550$, the matched sizes will be slightly reduced to 3.09 μm and 2.16 μm, respectively. The reduction in transverse size allows the witness bunch to approach the matched condition, thereby explaining why the ramping plasma configuration helps to preserve the emittance. Furthermore, figure 6 suggests that selecting the starting up-ramp point $z_{up} > 2$ cm is a safe choice to satisfy the emittance preservation condition within the acceptable tolerance.

4.3.3. Beam quality metrics

Parameter scan is typically a straightforward method for optimising beam quality. However, gaining a deeper physical understanding provides more valuable insight for effectively tuning the parameters. In this study, beam quality is characterised in terms of the remaining charge, energy spread, and normalised emittance.

Mismatched witness beams are prone to charge loss, particularly in the tail region as well as in the outer transverse regions, since electrons in these areas approach the bubble sheath more closely than others and are therefore subjected to defocusing forces in the dephasing regime. Electrons that are significantly deflected from the central axis are generally regarded as charge loss. Quantitatively, we apply a particle-cut criterion to include the majority of the beam data [10]. Electrons deviating beyond 5σ from the centre, defined by $r^2/2\sigma_r^2 + \xi^2/2\sigma_z^2 \leqslant 5^2/2$, are classified as charge loss, where $\xi = z—ct$ represents the co-moving coordinate.

Energy spread growth originates from non-uniform, phase-dependent acceleration. In principle, energy spread preservation benefits from a uniform accelerating gradient, e.g. the optimised beam loading effect discussed in section 4.2. However, conventional beam-loading-based methods typically mitigate the energy spread by tuning the bunch separation and shaping the charge profile of the witness bunch, both of which require precise control over the bunch. Therefore, a periodically modulated plasma density was proposed in [23], enabling alternating wakefield slopes that effectively suppresses the chirp evolution in the linear regime. In addition, since the non-uniform, phase-dependent acceleration occurs in both the transverse and longitudinal directions, the energy spread can be further optimised by reducing the bunch length and transverse size. Therefore, the smaller witness beam employed in this work benefits from the mitigation of non-uniform acceleration effects.

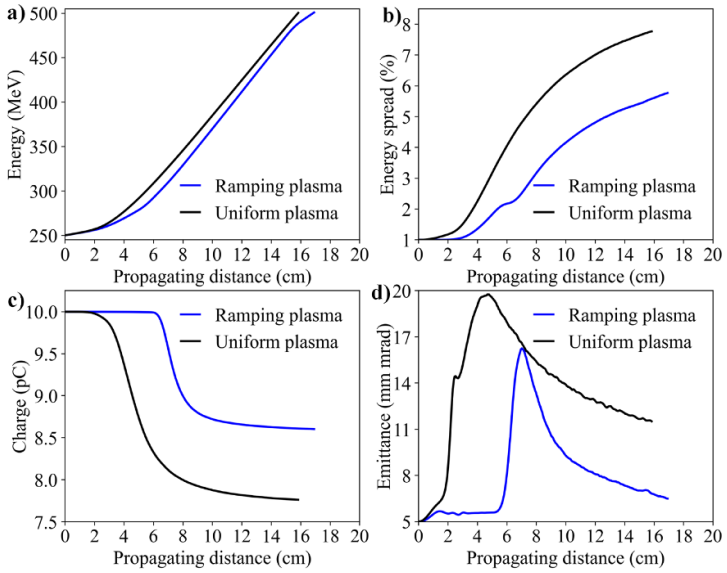

Figure 7. Beam quality evolution using different plasma density profiles for the longer witness bunch case. (a) Beam energy. (b) Energy spread. (c) Bunch charge. (d) Emittance. All data is collected within the 5σ range.

Normalised emittance, defined as

$$\epsilon_{N,x} = \sqrt{\langle x^2 \rangle \langle u_x^2 \rangle - \langle x u_x \rangle^2}, \tag{5}$$

where x is the offset from the nominal trajectory, and $u_x = p_x/p_z$ is the transverse momentum normalised by the longitudinal momentum. Here, p_x and p_z denote the horizontal transverse and longitudinal momentum components, respectively. The normalised emittance characterises the overall position-momentum variance and covariance of an electron beam in phase space [43]. Emittance growth has been well-documented in previous studies, where both defocusing and non-linear focusing forces play essential roles. For example, a mismatch between the bunch radius of the witness beam and the plasma density can induce strong off-axis deflections, increasing the position-momentum variance while reducing the covariance. Without applying a particle cut criterion, the dephased electrons expelled from the beam core can significantly deteriorate the emittance, even though they merely account for 1% or less of the total charge. Therefore, the emittance statistics in this study were also evaluated within the 5σ range.

4.3.4. Beam quality results

Figure 7 presents the beam quality evolution for the longer witness beam in uniform and ramping plasmas, respectively. Before $z \approx 2.5$ cm, where the acceleration occurs in the linear regime as mentioned in section 4.1, the energy growth for both cases is identical due to the use of the same driver beam. According to linear theory, for $n_b \ll n_0$, the maximum accelerating gradient is primarily determined by the driver beam (see equation (1)). In the non-linear regime, i.e. $z = 2.5$–5 cm, the uniform plasma exhibits a faster energy gain owing to its higher plasma density. Beyond this stage, i.e. $z = 5$–15 cm, both cases show nearly parallel energy growth rates, as shown in figure 7(a).

Figure 7(b) shows that the energy spread in the uniform plasma simulation begins to deviate from 1% before the end of the linear regime, whereas it remains preserved throughout the entire linear regime in the ramping plasma. Although both cases experience a significant increase in energy spread in the non-linear regime, the final values are 7.8% and 5.8% for the uniform and ramping plasmas, respectively, representing a 25% reduction in the ramping plasma.

Figure 7(c) illustrates the evolution of the witness bunch charge. In the uniform plasma, the bunch charge remains stable at the beginning but then decreases rapidly due to the defocusing phase of the dephasing regime, eventually reaching 7.75 pC (a 22.5% loss). In contrast, in the ramping plasma, the charge remains preserved up to $z \approx 6$ cm, at which the rear electrons of the witness beam touched the bubble sheath. Note that the onset of charge loss is delayed by ~ 1 cm, as a critical tolerance in λ_p must first be reached before entering the dephasing regime. The remaining non-dephasing charge stabilises at 8.60 pC, corresponding to a 14% loss.

In terms of emittance (see figure 7(d)), it rises from an initial 5 mm mrad to 19.7 mm mrad at $z \approx 4.7$ cm, at which it reaches a turning point. The emittance blowout can be attributed to a mismatch

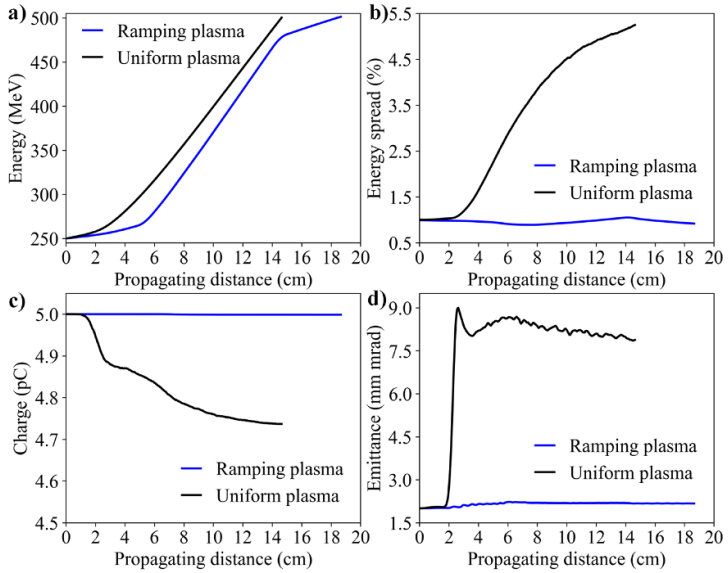

Figure 8. Beam quality evolution using different plasma density profiles for the shorter witness bunch case. (a) Beam energy. (b) Energy spread. (c) Bunch charge. (d) Emittance. All data is collected within the 5σ range.

between the transverse size of the witness beam and the plasma focusing, given by equation (3). As the transverse size continues to decrease and approaches the matched size, emittance recovery commences. However, the final emittance at the energy-doubling point reaches 11.5 mm mrad (a 130% growth), which is substantially higher than the initial value. In the ramping plasma, however, the emittance exhibits only a slight increase, as the transverse size still remains within the acceptable matching tolerance range [44]. Once the transverse size rises sharply beyond this tolerance, the emittance increases correspondingly. When the transverse size subsequently decreases towards the matching condition, the emittance decreases, ultimately reaching 6.5 mm mrad, corresponding to a 30% growth relative to the initial setting.

Figure 8 shows the evolution of the shorter witness-beam quality in uniform and ramping plasmas. In the uniform-plasma case, all three beam-quality indices remain stable in the linear regime. Once entering the non-linear regime, the energy spread begins to increase continuously, reaching a final value of 5.2%. Charge loss occurs throughout the non-linear regime, with 4.7 pC bunch charge remaining (a 6% loss), and the emittance grows to 7.88 mm mrad (a 294% growth) at the end. In contrast, with ramping plasma density, the corresponding final values are 0.92% for energy spread, 5.0 pC (no loss) for charge, and 2.17 mm mrad (an 8.5% growth) for emittance. In other words, both the energy spread and charge are effectively preserved. Although the emittance is not perfectly preserved, it shows a significant improvement compared with the uniform-plasma case.

In section 4.2, we proposed an ideal scenario to fully exploit both the positive-slope and negative-slope effects for energy-spread preservation. Figure 8(b) clearly demonstrates this behaviour, where the energy spread gradually grows to 1.1% during the high-density stage and ultimately reduces to 0.92% at the energy-doubling point. Compared with the periodically modulated plasma density method, we employ a single up-ramp and down-ramp plasma cell to improve experimental feasibility. Moreover, we demonstrate that the compensation of the energy gain remains effective even in the non-linear regime. It is worth noting that, for practical implementations, the length of the final plasma stage should be carefully optimised to ensure sufficient distance for reversing the energy-spread deterioration that occurs during the high-density plasma stage shown in figure 2.

4.3.5. Analysis of transverse size evolution

The bunch charge loss affects the completeness of the data, since the lost particles are no longer included in the transverse size calculation. Therefore, the evolution of the transverse size is correlated with the charge results shown in figures 7(c) and 8(c). Initially, the transverse wakefield acts to reduce the transverse size. However, the rear electrons experience the defocusing force while the front electrons are focused. In the linear regime, the focusing force counteracts the defocusing force, while in the nonlinear regime the focusing force dominates the overall beam dynamics, as illustrated in figures 3(b) and (c), respectively. Consequently, the overall transverse size remains nearly unchanged in the linear regime and

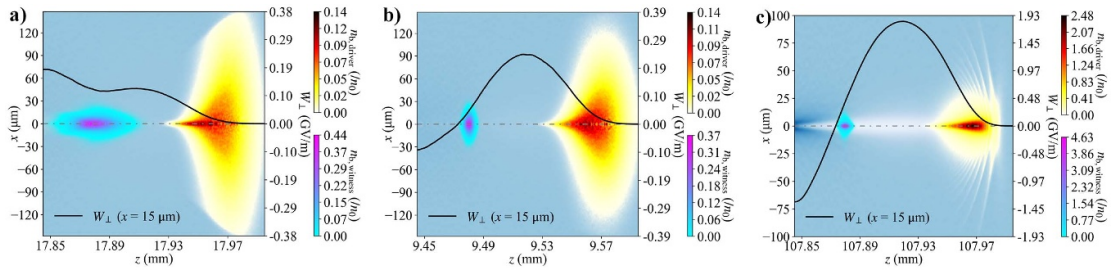

Figure 9. The off-axis ($x = 15\ \mu$m) transverse wakefield distribution at (a) $z = 17.97$ mm, longer witness bunch case, (b) $z = 9.57$ mm, shorter witness bunch case, and (c) $z = 107.97$ mm, shorter witness bunch case.

gradually decreases in the non-linear regime. As the rear electrons are expelled beyond the 5σ range, the remaining bunch begins to contract.

In the up-ramp plasma, the transverse size decreases sharply since the focusing phase fully includes the bunch, as shown in figure 9(a). The up-ramp plasma subsequently disturbs the equilibrium, causing the rear electrons to defocus. Meanwhile, the focused electrons maintain a stable transverse size and therefore the overall transverse-size variation is dominated by the defocusing component. Interestingly, a careful examination of the rising point at approximately $z = 5.3$ cm (see figure 6(a)), just before the onset of charge loss near $z = 6$ cm (see figure 7(c)), reveals the stage where the rear electrons are defocused but have not yet escaped beyond the 5σ boundary. Once the charge loss saturates, the transverse size begins to recover.

For the shorter witness bunch case in the uniform plasma, the initial defocusing effect dominates the transverse-size evolution until the charge loss virtually ceases, as shown in figures 9(b) and (c). In contrast, within the ramping plasma, no charge loss is observed throughout the energy-doubling process. All electrons remain focused, and the transverse size continues to decrease.

5. Conclusions

In this work, we presented the simulation results of the plasma-beam interaction based on the FEBE specifications. Results show that the energy doubling within a 20-cm-long plasma cell while maintaining high beam quality is achieved. The interaction between the driver and plasma initially occurs in the linear regime, followed by a transition to the non-linear regime at $z \approx 2.5$ cm. The beam loading effect has been observed. With coupled plasma density ramps employed, the transverse wakefield can initially include the entire witness beam. As a result, the charge is well preserved, and the reduced transverse size approaches the matching condition, thereby preserving low emittance. The optimised plasma-length configuration effectively regulates the positive- and negative-slope effects of beam loading, leading to energy spread preservation. The longer witness beam exhibits a significant improvement in beam quality compared with the uniform plasma case, while all three beam-quality indices of the shorter witness beam are preserved. These findings provide valuable insights for proof-of-principle energy-doubling experiments with beam-quality preservation, which are of great relevance to future applications, such as for high-energy physics, compact light sources, and industrial applications.

Acknowledgments

The authors would like to acknowledge the support from the Cockcroft Institute Core Grant No. ST/V001612/1 and the computing resources provided by the STFC Scientific Computing Department's SCARF cluster.

Data availability statement

All data that support the findings of this study are included within the article (and any supplementary files).

Author contributions

Jiaqi Zhang 0000-0001-9367-8387
Conceptualization (equal), Data curation (lead), Formal analysis (lead), Investigation (lead), Methodology (lead), Software (lead), Visualization (lead), Writing – original draft (lead)

Deepa Angal-Kalinin 0000-0001-5727-3526
Resources (equal), Writing – review & editing (supporting)

Oznur Apsimon 0000-0002-5410-7706
Writing – review & editing (equal)

Stewart Boogert
Funding acquisition (lead), Project administration (equal), Resources (equal)

Richard D'Arcy
Writing – review & editing (equal)

James Jones 0000-0003-3510-6721
Resources (equal), Writing – review & editing (equal)

Toby Overton 0000-0003-1297-2213
Writing – review & editing (supporting)

Thomas Pacey 0000-0002-4240-5888
Resources (equal), Writing – review & editing (supporting)

Hossein Saberi 0000-0002-8938-9934
Conceptualization (equal), Software (supporting), Writing – review & editing (equal)

Guoxing Xia 0000-0002-3683-386X
Funding acquisition (equal), Project administration (equal), Supervision (lead), Validation (lead), Writing – review & editing (lead)

References

[1] Tajima T and Dawson J M 1979 *Phys. Rev. Lett.* **43** 267
[2] Muggli P and Hogan M J 2009 *C. R. Phys.* **10** 116–29
[3] Wilson T, Farmer J, Pukhov A, Sheng Z M and Hidding B 2024 *Phys. Rev. Accel. Beams* **27** 071301
[4] Litos M *et al* 2014 *Nature* **515** 92–95
[5] Rosenzweig J B, Cline D, Cole B, Figueroa H, Gai W, Konecny R, Norem J, Schoessow P and Simpson J 1988 *Phys. Rev. Lett.* **61** 98
[6] Blumenfeld I *et al* 2007 *Nature* **445** 741–4
[7] Muggli P, Allen B, Yakimenko V, Park J, Babzien M, Kusche K and Kimura W 2010 *Phys. Rev. Spec. Top. Accel. Beams* **13** 052803
[8] Clarke C *et al* 2012 Facet: slac's new user facility *Proc. of IPAC2012* (*New Orleans, Louisiana, USA*) vol 23 pp 2741–3 (available at: https://digital.library.unt.edu/ark:/67531/metadc836667/)
[9] Schröder S *et al* 2020 *J. Phys.: Conf. Ser.* **1596** 012002
[10] Romeo S *et al* 2018 *Nucl. Instrum. Methods Phys. Res.* A **909** 71–75
[11] Svensson J B, Andersson J, Ferri J, Charles T, Ekerfelt H, Mansten E, Thorin S and Lundh O 2022 *Nucl. Instrum. Methods Phys. Res.* A **1033** 166591
[12] D'Arcy R *et al* 2019 *Phil. Trans. R. Soc.* A **377** 20180392
[13] Prat E *et al* 2019 *Phys. Rev. Lett.* **123** 234801
[14] Angal-Kalinin D, Boogert S and Jones J K 2024 *Front. Phys.* **12** 1496850
[15] Esarey E, Schroeder C B and Leemans W P 2009 *Rev. Mod. Phys.* **81** 1229–85
[16] Lee S, Katsouleas T, Hemker R, Dodd E and Mori W 2001 *Phys. Rev.* E **64** 045501
[17] Jain A, Yoffe S R, Ersfeld B, Holt G K, Gupta D N and Jaroszynski D A 2024 *Sci. Rep.* **14** 19127
[18] Braunmüller F *et al* 2020 *Phys. Rev. Lett.* **125** 264801
[19] Martinez De La Ossa A, Hu Z, Streeter M, Mehrling T, Kononenko O, Sheeran B and Osterhoff J 2017 *Phys. Rev. Accel. Beams* **20** 091301
[20] Mehrling T J 2014 Theoretical and Numerical Studies on the Transport of Transverse Beam Quality in Plasma-Based Accelerators *PhD Thesis* University of Hamburg (available at: https://ediss.sub.uni-hamburg.de/handle/ediss/5644)
[21] Mehrling T, Fonseca R, Martinez de la Ossa A and Vieira J 2019 *Phys. Rev. Accel. Beams* **22** 031302
[22] Ariniello R, Doss C, Lee V, Hansel C, Cary J and Litos M 2022 *Phys. Rev. Res.* **4** 043120
[23] Brinkmann R *et al* 2017 *Phys. Rev. Lett.* **118** 214801
[24] Snedden E *et al* 2024 *Phys. Rev. Accel. Beams* **27** 041602
[25] Lehe R, Kirchen M, Andriyash I A, Godfrey B B and Vay J L 2016 *Comput. Phys. Commun.* **203** 66–82
[26] Godfrey B B 1974 *J. Comput. Phys.* **15** 504–21
[27] Buneman O, Barnes C, Green J and Nielsen D 1980 *J. Comput. Phys.* **38** 1–44
[28] Barbera Ramos M, Xia G, Bonatto A, Martín-Luna P, Resta-Lopez J, Apsimon O, Rodin V and Bontoiu C 2023 *JACoW IPAC2023* 1457–60

[29] Kurz T et al 2021 Nat. Commun. 12 2895
[30] Marocchino A, Chiadroni E, Ferrario M, Mira F and Rossi A R 2018 Nucl. Instrum. Methods Phys. Res. A 909 408–13
[31] Esarey E, Sprangle P, Krall J and Ting A 1996 IEEE Trans. Plasma Sci. 24 252–88
[32] Olsen V K B, Adli E and Muggli P 2018 Phys. Rev. Accel. Beams 21 011301
[33] Grebenyuk J, de la Ossa A M, Mehrling T and Osterhoff J 2014 Nucl. Instrum. Methods Phys. Res. A 740 246–9
[34] Filippi F, Anania M, Biagioni A, Chiadroni E, Cianchi A, Ferrario M, Mostacci A, Palumbo L and Zigler A 2016 J. Instrum. 11 C09015
[35] Crincoli L et al 2024 J. Phys.: Conf. Ser. 2687 042006
[36] Arjmand S et al 2023 J. Phys.: Conf. Ser. 2439 012012
[37] Garland J, et al 2020 arXiv:2010.02567
[38] Gonsalves A et al 2015 Proc. 6th Int. Particle Accel. Conf. 1319–24
[39] Xia G et al 2014 Nucl. Instrum. Methods Phys. Res. A 740 165–72
[40] Vafaei-Najafabadi N 2016 Experimental Investigations of Beam Driven Plasma Wakefield Accelerators PhD thesis University of California (available at: https://escholarship.org/uc/item/2xn3m59r)
[41] Rosenzweig J, Andonian G, Ferrario M, Muggli P, Williams O, Yakimenko V and Xuan K 2010 AIP Conf. Proc. 1299 500–4
[42] Tzoufras M, Lu W, Tsung F S, Huang C, Mori W B, Katsouleas T, Vieira J, Fonseca R and Silva L O 2008 Phys. Rev. Lett. 101 145002
[43] Lindstrøm C A et al 2024 Nat. Commun. 15 6097
[44] Farmer J, Liang L, Ramjiawan R, Velotti F, Weidl M, Gschwendtner E and Muggli P 2022 arXiv:2203.11622